

Minkowski Functionals of Abell/ACO Clusters

M. Kerscher¹, J. Schmalzing¹, J. Retzlaff², S. Borgani^{3,4}, T. Buchert¹,
S. Gottlöber², V. Müller², M. Plionis^{4,5} & H. Wagner¹

¹*Sektion Physik, Ludwig-Maximilians-Universität, Theresienstr. 37, D-80333 München, Germany*

²*Astrophysikalisches Institut Potsdam, An der Sternwarte 16, D-14482 Potsdam, Germany*

³*INFN Sezione di Perugia, c/o Dipartimento di Fisica dell'Università, via A. Pascoli, I-06100 Perugia, Italy*

⁴*SISSA – International School for Advanced Studies, via Beirut 2–4, I-34013 Trieste, Italy*

⁵*National Observatory of Athens, Lofos Nimfon, Thessio, 18110 Athens, Greece*

submitted to MNRAS

ABSTRACT

We determine the Minkowski functionals for a sample of Abell/ACO clusters, 401 with measured and 16 with estimated redshifts. The four Minkowski functionals (including the void probability function and the mean genus) deliver a global description of the spatial distribution of clusters on scales from 10 to $60h^{-1}$ Mpc with a clear geometric interpretation. Comparisons with mock catalogues of N-body simulations using different variants of the CDM model demonstrate the discriminative power of the description. The standard CDM model and the model with tilted perturbation spectrum cannot generate the Minkowski functionals of the cluster data, while a model with a cosmological constant and a model with breaking of the scale invariance of perturbations (BSI) yield compatible results.

Key words: cosmology – large scale structure – statistical methods – structure formation

1 INTRODUCTION

The distribution of galaxy clusters has been used for a long time as a useful tracer of the large-scale structure of the Universe and as a constraint for cosmological models. To present knowledge, clusters of galaxies represent the largest gravitationally bound entities in the hierarchy of cosmic structures. In addition, their amplified clustering, with respect to that of galaxies, can be reliably measured on large scales ($> 20h^{-1}$ Mpc) where the gravitational evolution still keeps track of the initial fluctuation spectrum.

The first quantitative analyses of the cluster distribution date back to the pioneering works by Bahcall & Soneira (1983) and Klypin & Kopylov (1983) and were based on the estimate of the cluster 2-point correlation function, $\xi_{cc}(r)$. Although dealing with a rather limited number of objects, these analyses clearly showed that Abell (1958) clusters have a clustering scale length r_0 , defined by $\xi_{cc}(r_0) = 1$, which is much larger than that of galaxies. Considerable observational effort has been made to improve the large-scale mapping of the cluster distribution. Analyses based on the extension of the Abell sample to the southern hemisphere (Abell, Corwin & Olowin 1989, hereafter ACO) and on progres-

sively larger redshift compilations of Abell and ACO clusters (e.g. Postman, Geller & Huchra 1992) basically confirmed the original result that $r_0 \simeq 20h^{-1}$ Mpc (see also Cappi & Maurogordato 1992; Plionis, Valdarnini & Jing 1992; Peacock & West 1992). On the other hand, new samples based on more objective cluster identification criteria, both in the optical (Dalton et al. 1994; Collins et al. 1994) and in the X-ray (e.g. Nichol, Briel & Henry 1994; Romer et al. 1994) bands, revealed a smaller length scale, $r_0 \simeq 13 \dots 16h^{-1}$ Mpc. This difference might be ascribed to richness contamination from projection effects of the Abell/ACO samples (Sutherland 1988, see also Jing, Plionis & Valdarnini 1992) or to the richness-clustering dependence (Bahcall & West 1992). In any case, the standard CDM model fails to predict the large range of positive cluster correlation function ($\xi(r) > 0$ up to scales of $70h^{-1}$ Mpc, see White et al. 1987, Olivier et al. 1993).

Although several further analyses have been devoted to compare data on the cluster distribution to the predictions of a variety of DM models (e.g. Bahcall & Cen 1992; Dalton et al. 1994; Borgani et al. 1995), most of them have been mainly based on low-order statistics. A more complete description of the cluster distribution requires the use of higher-order statistics, which are ca-

pable of capturing global aspects of the clustering. One example is the genus statistics applied to the cluster data by Rhoads, Gott & Postman (1994) and by Pearson et al. (1996).

A direct measurement of properties of a general point distribution can be made using Minkowski functionals (Mecke, Buchert & Wagner 1994). These measures provide a morphological (geometrical and topological) description of the point distribution and comprise information about correlation functions of arbitrary order. Application to clusters of galaxies is especially promising since clusters bear direct contact to the formation of the largest structures in the universe. As geometrical characteristics of structure, the Minkowski functionals combine both the advantage of intuitive interpretation of their meaning and the advantage of delivering a quantitative measure. The aim of this paper is to apply the Minkowski functional statistics in order to compare an extended redshift sample of Abell/ACO clusters with mock catalogues obtained from large PM N-body simulations, starting from different models for the initial power spectrum. To this purpose, we extract artificial cluster samples from the simulations, thereby reproducing the main characteristics of the observational data set (cluster number density, boundary geometry, selection functions for galactic absorption and luminosity effects).

Simulations are run for the Standard Cold Dark Matter (SCDM) model, a ‘Tilted’ CDM model (TCDM) with $\nu = 0.9$ for the post-inflationary spectral index, a low-density CDM model with $\Omega_0 = 0.35$ and a cosmological constant (Λ CDM), and a double inflation model with Broken Scale Invariance (BSI) of the primordial perturbation spectrum. It is generally accepted that the SCDM spectrum fails to reproduce the cluster correlation amplitude and, once normalized on large scales to match the CMB anisotropies, it largely overproduces clusters. These shortcomings are interpreted as the consequence of the wrong shape of the SCDM spectrum (see, e.g., Borgani et al. 1996; Mo, Jing & White 1996). As a possible remedy, Λ CDM modifications of the SCDM model suitably change the spectrum shape at the cost of introducing one additional parameter in comparison to SCDM, while the TCDM model and the BSI model change the shape of the power spectrum by introducing one and two additional parameters, respectively.

A brief description of the observational data is provided in Section 2. In Section 3 we present the cosmological models on which simulations are based and sketch the procedure for cluster selection and mock catalogue construction. We define and discuss in Section 4 the properties of Minkowski functionals, relations to other statistics, the method of analysis and its results. In Section 5 we summarize and draw our conclusions.

2 OBSERVATIONAL DATA

We consider an extended redshift sample of Abell and ACO clusters with richness $R \geq 0$ (Abell 1958; Abell, Corwin & Olowin 1989). In the following we will pro-

vide only a brief description of this sample since more details are given in Borgani et al. (1996; see also Plionis & Valdarnini 1995). The northern (Abell) part of the sample, with declination $\delta \geq -17^\circ$, is defined by those clusters that have measured redshift $z \leq 0.1$, while the southern ACO part, with $\delta < -17^\circ$, is defined by those clusters with $m_{10} < 17$, where m_{10} is the magnitude of the tenth brightest cluster galaxy in the magnitude system corrected according to Plionis & Valdarnini (1991).

The effect of galactic absorption is modelled according to the standard cosecant dependence on the galactic latitude b ,

$$P(|b|) = 10^{\alpha(1 - \csc |b|)}, \quad (1)$$

with $\alpha \approx 0.3$ for the Abell sample (Bahcall & Soneira 1983; Postman et al. 1989) and $\alpha \approx 0.2$ for the ACO sample (Batuski et al. 1989). In order to limit the effects of galactic absorption we only use clusters with $|b| \geq 30^\circ$.

The cluster-redshift selection function $P(z)$ is determined by fitting the cluster density as a function of z :

$$P(z) = \begin{cases} 1 & \text{if } z \leq z_c, \\ A \exp(-z/z_o) & \text{if } z > z_c, \end{cases} \quad (2)$$

where $A = \exp(z_c/z_o)$, and z_c is the redshift below which the spatial density of clusters remains constant (volume-limited sample). We find $z_c \approx 0.078$, $z_o \approx 0.012$ and $z_c \approx 0.068$, $z_o \approx 0.014$ for Abell and ACO samples, respectively. Since the exponential decrease of $P(z)$ can introduce considerable shot noise errors at large redshifts, we prefer to limit our analysis to $r_{\max} = 240 h^{-1} \text{Mpc}$, where the catalogue is approximately volume limited.

There are in total 417 Abell/ACO clusters fulfilling the above criteria: 262 Abell clusters with measured redshifts, and 155 ACO clusters, 16 of which have z estimated from the m_{10} - z relation calibrated by Plionis & Valdarnini (1991). These numbers correspond to $\langle n \rangle_{\text{Abell}} = (1.6 \pm 0.25) \times 10^{-5} (h^{-1} \text{Mpc})^{-3}$ and $\langle n \rangle_{\text{ACO}} = (2.3 \pm 0.3) \times 10^{-5} (h^{-1} \text{Mpc})^{-3}$, for the Abell and ACO cluster number densities, respectively, once corrected for galactic absorption according to eq. (1). The density difference is mostly spurious, due to the higher sensitivity of the IIIa-J emulsion plates on which the ACO survey is based. The above density values correspond to average cluster separations of $\langle d_{\text{Abell}} \rangle \simeq 40 h^{-1} \text{Mpc}$ and $\langle d_{\text{ACO}} \rangle \simeq 35 h^{-1} \text{Mpc}$.

3 MOCK SAMPLES FROM N-BODY SIMULATIONS

3.1 Cosmological models

We simulated the evolution of large-scale structure in four different types of spatially flat Cold Dark Matter models. They are listed below.

(a) The Standard CDM (SCDM) model with $\Omega_0 = 1$ and $h = 0.5$ for the Hubble constant in units of $100 \text{ km s}^{-1} \text{ Mpc}^{-1}$, which we take as a standard of reference.

(b) A tilted CDM (TCDM) model, with $\nu = 0.9$ for the post-inflationary spectral index as arising, for instance, from power law inflation.

(c) A low-density CDM (Λ CDM) model, with $\Omega_0 = 0.35$, $h = 0.7$ and spatial flatness restored by a cosmological constant term $\Omega_\Lambda = 0.65$.

(d) A Broken Scale-Invariance (BSI) CDM model, which exhibits a step-like primordial spectrum due to a double-inflationary scenario. The modification of the power spectrum is specified by two parameters, the step location at $k_{\text{break}}^{-1} = 1.5 h^{-1} \text{Mpc}$ and its relative height $\Delta = 3$. With this parameter choice, the model provides a good fit to a variety of observational data (Gottlöber, Mücke & Starobinsky 1994, Amendola et al. 1995, Kates et al. 1995, Ghigna et al. 1996).

For the CDM model we use the transfer function as parameterized by Bardeen et al. (1986), which assumes a vanishing baryon contribution. Although the presence of baryons is relevant as far as small-scale properties ($\lesssim 5 h^{-1} \text{Mpc}$) are concerned, it has negligible influence on the large-scale clustering ($\gtrsim 10 h^{-1} \text{Mpc}$), which we want to investigate using galaxy clusters. We summarize the main model parameters in Table 1. The power spectra are normalized according to the two year COBE-DMR 53 and 90 GHz galactic sky maps following the prescription of Górski et al. (1994) for the $\Omega = 1$ models and of Stompor, Górski & Banday (1995) for the Λ CDM model.

We did not take into account any possible gravitational wave contributions for the BSI and TCDM model. We have also done our analysis for the one year COBE normalization and verified that the statistics of the cluster distribution are insensitive to this reduction of the spectrum amplitude (see also Croft & Efstathiou 1994; Borgani et al. 1995). Therefore, any uncertainty either in our normalization procedure or in the measured level of CMB temperature anisotropy has no effect on the final results of the analysis. In particular, our results will not change when adopting a power spectrum normalization compatible with the 4 year COBE data (see, e.g., Bennett et al. 1996). This normalization would imply a reduction of the fluctuation amplitude σ_8 by about 11 % for all the models under consideration.

The spectra we used in our simulations are shown in Figure 1, where the horizontal bar selects the part of the spectrum between the inverse box size and the Nyquist frequency which is realized in the simulation.

We evolve the initial density field starting from redshift $z = 25$ until the present epoch employing a standard PM N-body scheme with $N_p = 300^3$ particles ($m_{par} = 1.3 \times 10^{12} h^{-1} M_\odot$) and $N_g = 600^3$ grid cells in a simulation box of $L = 500 h^{-1} \text{Mpc}$ comoving length a side. This provides a spatial resolution of $\simeq 1.7 h^{-1} \text{Mpc}$ (two cells). We suppose that the simulation box is large enough to contain all fluctuation modes which contribute to the large-scale cluster clumping. In order to account for the effect of statistical variance, we carried out simulations for four random realizations for SCDM and three for Λ CDM, respectively, while one realization was done for TCDM and BSI.

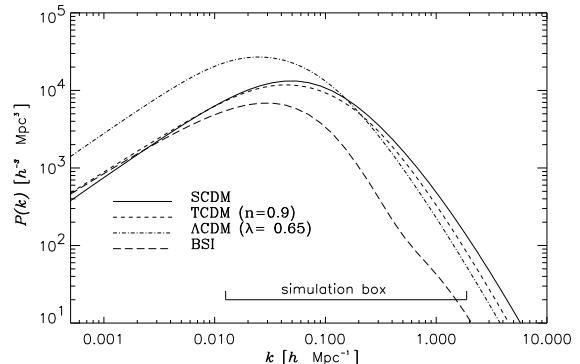


Figure 1. The SCDM, TCDM, Λ CDM and BSI power spectra. The bar selects the wavenumber range corresponding to the adopted box size of $500 h^{-1} \text{Mpc}$.

Table 1. Summary of model parameters

Model	h	Ω_0	Ω_Λ	ν	σ_8
SCDM	0.5	1	0	1	1.37
TCDM	0.5	1	0	0.9	1.25
Λ CDM	0.7	0.35	0.65	1	1.30
BSI	0.5	1	0	-	0.60

3.2 Mock cluster samples

We identify clusters from the final particle distribution by applying an iterative procedure to the high peaks of the density field reconstructed on the 600^3 mesh points (see also Klypin & Rhee 1994). After assigning the density field on the grid through a cloud-in-cell interpolating scheme, we identify those points which correspond to local density maxima. Afterwards, we center a sphere of radius $1.5 h^{-1} \text{Mpc}$, corresponding to the Abell radius, on each of these local maxima and compute the center of mass position for all the particles falling within that sphere. This position is used as the new cluster center and the procedure is repeated until convergence. We find that in general only a few (about 5) iterations are required for the cluster coordinates and masses to converge to their final values.

From the resulting list of candidate clusters, we select the N_{cl} most massive objects and identify them with Abell/ACO clusters. By definition, $N_{cl} = (L/d_{cl})^3$ is the expected number of clusters within the simulation box, having mean separation d_{cl} .

In order to check the robustness of our cluster identification scheme, we also based their identification on the friend-of-friend algorithm, with linking length $b = 0.2$ times the mean particle separation (e.g. Frenk et al. 1988). This value of b defines groups bounded by an isodensity surface of about 125 times the average density and, therefore, to an average internal overdensity of about 180 if an isothermal density profile is assumed (e.g. Lacey & Cole 1994). Such an overdensity is very close to the value expected for a virialized structure resulting from the spherical top-hat collapse (e.g. Peebles

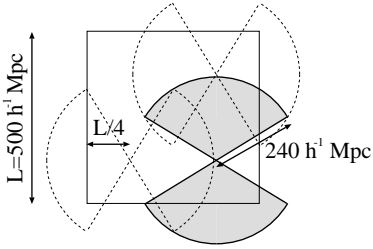


Figure 2. Projected positions of three mock samples in the simulation box, showing their overlap.

1980). We will show elsewhere that the cluster distributions obtained with these two procedures are very similar not only in a statistical sense, but also as far as the point-to-point comparison of the cluster positions is concerned.

After generating the cluster distribution in the simulation box, we extract mock samples which reproduce the same observational features as the real Abell/ACO sample. In each box we locate 8 observers along the main diagonal axes, each having a distance of $L/4 = 125 h^{-1} \text{Mpc}$ from the three closest faces. First we include all clusters up to a maximum distance of $240 h^{-1} \text{Mpc}$ in each mock sample (see Figure 2, the simulation box has periodic boundaries). We then randomly sample them to get a density distribution reproducing the observational selection functions for galactic absorption and redshift extinction (see also Borgani et al. 1996). In order to minimize the overlap between mock samples, the coordinate systems for two adjacent observers are chosen so that the corresponding galactic planes are orthogonal to each other. Even with this choice, it turns out that different mock samples involve overlapping volumes and, therefore, they cannot be considered as completely independent.

Minkowski functionals are sensitive to the number density. In the case of a Poisson process one may easily derive scaling relations with the number density and radius using the analytical results of Mecke & Wagner (1991) and the homogeneity property of the Minkowski functionals, $M_\mu(\lambda A_r) = \lambda^{d-\mu} M_\mu(A_r)$, ($\mu = 0, \dots, 3$) with a positive real scaling factor λ (see Section 4 for the definition of the functionals M_μ of A_r produced by balls B_r of radius r around each cluster). For generic distributions no scaling relations are available since the scaling properties depend, even without correlations, on the dimensionality of the support of the point process. Therefore, care has to be taken to reproduce in the simulated samples the correct number of Abell and ACO clusters separately. To this purpose, after generating a mock sample, we randomly degrade the cluster number density in the Abell part until the number density reaches a fraction $\langle n \rangle_{\text{Abell}} / \langle n \rangle_{\text{ACO}}$ of the number density of the ACO part. Since the overall number density is fixed in the whole simulation box, different samples may contain different numbers of clusters, with fluctuations around 10% and deviations of single samples as large as 30%. Instead of forcing all the samples to have the same number of clusters as the real one, we prefer to main-

Table 2. The Minkowski functionals in three-dimensional space expressed in terms of the corresponding geometric quantities.

	geometric quantity	μ	M_μ
V	volume	0	V
A	surface	1	$A/8$
H	integral mean curvature	2	$H/2\pi^2$
χ	Euler characteristic	3	$3\chi/4\pi$

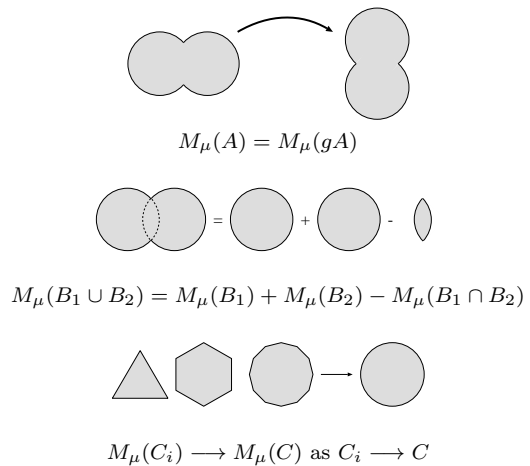


Figure 3. Minkowski functionals are unique descriptors of morphology under the requirements of Motion Invariance (A), Additivity (B) and Continuity (C).

tain such fluctuations and consider them as an effect of cosmic variance. We only take care that, after averaging over the eight observers in each box, the resulting average cluster number per sample reproduces the observational one. We find that choosing a mean cluster separation $d_{cl} = 36 h^{-1} \text{Mpc}$, which roughly corresponds to the average separation of ACO clusters, always produces an average number of Abell and ACO clusters per sample which differs by $\lesssim 5\%$ from the corresponding numbers of the observational case.

As we will see, uncertainties in the analysis of the Minkowski functionals are largely dominated by the observer-to-observer scatter within the same box, which is due to the fluctuations in the cluster number density. The box-to-box variance of different simulations, which accounts for the sampling of independent patches of the Universe is significantly smaller.

4 ANALYSIS USING MINKOWSKI FUNCTIONALS

4.1 Definition and general properties

Let us consider the set of points supplied by cluster positions in three-dimensional space. We decorate each point with a ball of radius r , thereby creating connections between neighbouring balls. We now wish to in-

investigate how the global morphology of the union set of these balls changes with the radius r , which is employed as a (single) diagnostic parameter. To achieve this, we need quantitative measures of geometry and topology for bodies in three-dimensional space.

It seems sensible to request that such measures be motion invariant valuations of the bodies, i.e. scalar functionals satisfying additivity and invariance under rotations and translations, as well as a continuity requirement (see Figure 3). The theorem of Hadwiger (Hadwiger 1957) tells us that in three dimensions any functional satisfying these requirements is a linear combination of the four Minkowski functionals. In this sense the four Minkowski functionals supply a complete and unique characterization of global morphology in three dimensions. Table 2 displays their direct relation to morphological quantities known from differential geometry. For a smooth body K , they are given as surface integrals of functions of the principal curvature radii R_1 , R_2 :

$$\begin{aligned} A &= \int_{\partial K} dA, \\ H &= \frac{1}{2} \int_{\partial K} dA \left(\frac{1}{R_1} + \frac{1}{R_2} \right), \\ \chi &= \frac{1}{4\pi} \int_{\partial K} dA \frac{1}{R_1 R_2}. \end{aligned} \quad (3)$$

(for a rigorous derivation of these relations see Mecke, Buchert & Wagner 1994). A good overview and extensive references on integral geometry are given in an article by Weil (1983) or in the recent book by Schneider (1993). For further details on Minkowski functionals in the cosmological context see Mecke (1994), Buchert (1995), Platzöder & Buchert (1995), Schmalzing, Kerscher & Buchert (1995) and especially Mecke, Buchert & Wagner (1994).

4.2 Boundary correction

For Minkowski functionals there is a concise way of dealing with boundaries (Mecke & Wagner 1991). Let D be the window (the sample geometry) through which we look at N clusters. $A_r = \bigcup_{i=1}^N B_r(i)$ is the union of balls $B_r(i)$ of radius r centered on the i -th cluster, respectively. In order to obtain a precise quantitative measure of the boundary contribution we have to calculate the Minkowski functionals $M_\mu(A_r \cap D)$ of the intersection of the union of all balls with the window, and the Minkowski functionals $M_\mu(D)$ of the window itself, as illustrated in Figure 4. The quantities $M_\mu(A_r \cap D)$ are well suited for the analysis of redshift catalogues but we can go further.

Following Mecke & Wagner (1991) and Schmalzing, Kerscher & Buchert (1995), we can extract the volume densities of the Minkowski functionals $m_\mu(A_r)$ from the catalogue if the window contains a fair sample of an ergodic and stationary point process. The boundary con-

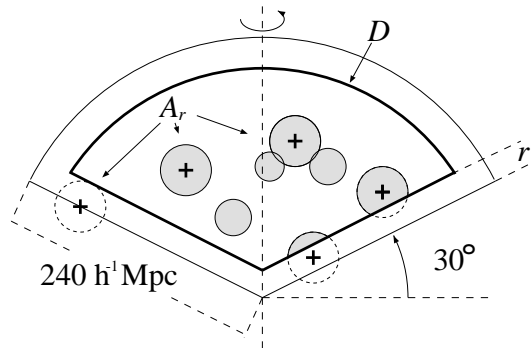


Figure 4. Two-dimensional cut through the geometry of one part. The shaded area is the set $A_r \cap D$, in this case D is the overall sample geometry (thin line) shrunk by r .

tribution of the window is then completely removed by applying the following recursive formula:^{*}

$$m_\mu(A_r) = \frac{M_\mu(A_r \cap D)}{M_0(D)} - \sum_{\nu=0}^{\mu-1} \binom{\mu}{\nu} m_\nu(A_r) \frac{M_{\mu-\nu}(D)}{M_0(D)}. \quad (4)$$

Fava & Santaló (1979) give a mathematically rigorous derivation of this formula. In the case of periodic boundary conditions we have $M_\nu(D) = 0$ for $\nu \in \{1, 2, 3\}$ and therefore $m_\mu(A_r) = M_\mu(A_r \cap D)/M_0(D)$ for $\mu \in \{0, 1, 2, 3\}$. Generally, for $\mu = 0$, the formula is trivial. We get for the volume density $m_0(A_r)$ (and for the void probability function, see below)

$$m_0(A_r) = \frac{M_0(A_r \cap D)}{M_0(D)}. \quad (5)$$

Thus, for the removal of boundary contributions of the Euler characteristic (and hence the genus, see below) in a window D with arbitrary non-periodic boundaries one needs to know *all* the Minkowski functionals. Coles, Davies & Pearson (1996) proposed a method for calculating the genus of isodensity surfaces based on the Morse theorem. Their boundary correction is exact for periodic cubes.

4.3 Connection to other statistics

The most notable Minkowski functional is the Euler characteristic χ whose investigation has become a standard method of cosmology known as genus-statistics (see e.g. Gott, Weinberg & Melott 1987, Melott 1990). In three dimensions, for a single body B the Euler characteristic $\chi(B)$ is related to the genus g of the surface ∂B by

$$\chi(B) = \frac{1}{2} \chi(\partial B) = \frac{1}{2} (1 - g). \quad (6)$$

The genus is usually calculated from the integral Gaussian curvature of smoothed isodensity surfaces. The con-

^{*} we use the convention $\sum_{n=i}^j x_n = 0$ for $j < i$

struction of the isodensity surface involves two parameters, the smoothing length and the density threshold. In our model we employ the radius as a single diagnostic scale parameter. For simulation data, with periodic boundaries, the construction of the density field is straightforward; for redshift surveys one has to rely on boundary corrections (Rhoads, Gott & Postman 1994). Since we do not need the density field in our analysis we are not concerned with these additional (empirical) corrections.

Another well known statistic is the void probability P_0 (see White 1979) which is directly related to the volume density m_0 according to

$$1 - P_0(r) = m_0(A_r). \quad (7)$$

Similar to the connection of the void probability with the hierarchy of correlation functions (see Stratonovich 1963 and White 1979), one finds analogous expressions for all Minkowski functionals (Mecke 1994, Mecke, Buchert & Wagner 1994).

There is a rule of thumb stating that the first zero of the Euler characteristic serves as an estimate for the percolation threshold (Mecke & Wagner 1991).

The dependence of the volume $M_0(A_r)$ on the radius r allows the calculation of the Minkowski-Bouligand dimension D_M

$$D_M = 3 - \lim_{r \rightarrow 0} \frac{\log(M_0(A_r))}{\log(r)} \quad (8)$$

which is equal to the capacity (box counting) dimension, giving an upper limit to the Hausdorff dimension (see Falconer 1990). As in the case of the ordinary box-counting method, any estimate of D_M based on a finite number of points is affected by discreteness problems, as discussed by Borgani et al. (1993) and Dubrulle & Lachièze-Rey (1994).

4.4 Analysis of the Abell/ACO catalogue

In order to calculate the densities of Minkowski functionals from the Abell/ACO sample, we analyzed the northern and southern part separately. Then we calculated the average between these two parts; since they do not intersect, this gives the same results as analyzing both parts together. In Figure 4 we sketch the geometry of one part. At each radius r , the walls of the original window are shrunk by the radius r . All clusters within the original window contribute, but clusters lying outside the original window do not. We can then apply the boundary removal described in Subsection 1 for each radius separately to recover the densities $m_\mu(A_r)$ of the Minkowski functionals. Figures 5, 6 and 7 display these densities for the various processes described above.

According to their definition, the densities of the Minkowski functionals are expressed in the following units:

$$\begin{aligned} [m_0] &= 1, & [m_1] &= (h^{-1}\text{Mpc})^{-1}, \\ [m_2] &= (h^{-1}\text{Mpc})^{-2}, & [m_3] &= (h^{-1}\text{Mpc})^{-3}. \end{aligned}$$

In Figure 5 we plot the densities of the Minkowski functionals for both the Abell/ACO sample (solid lines) and a Poisson process (shaded area). Although the mean

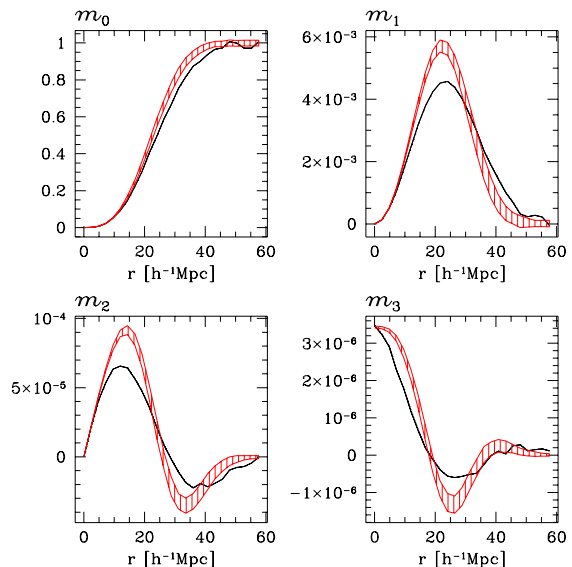


Figure 5. Densities of the Minkowski functionals for the Abell/ACO (average of northern and southern parts) and a Poisson process (shaded area) with the same number density. The shaded area gives the statistical variance of the Poisson process calculated from 100 different realizations.

values for the Poisson process are known analytically (Mecke & Wagner 1991), in Figure 5 we preferred to compute numerically the mean values and the standard errors of the Minkowski functionals for 100 realizations of such a Poisson process within the sample geometry.

The most prominent feature of all four Minkowski functionals are the broader extrema for the Abell/ACO data as compared to the results for the Poisson process. This is a first indication for enhanced clustering. Let us now look at each functional in detail.

The Minkowski functional m_0 measures the density of the covered volume. On scales between $25 h^{-1}\text{Mpc}$ and $40 h^{-1}\text{Mpc}$, m_0 as a function of r lies slightly below the Poisson data. The volume density is lower because of the clumping of clusters on those scales. It is remarkable that this behaviour occurs in the spatial region where clusters are weakly clumped as measured by the conventional two-point autocorrelation function (the region where $0 < \xi(r) < 1$). The Minkowski functionals involve correlation functions of every order (see Section 4.3) and therefore are more sensitive to enhanced clumping.

The Minkowski functional m_1 measures the surface density of the coverage. It has a maximum at about $20 h^{-1}\text{Mpc}$ both for the Poisson sample and for the cluster data. This maximum is due to the granular structure of the union set on the relevant scales. At the same scales, we find the maximum deviation from the Poisson distribution. The lower values of the cluster data m_1 with respect to the Poisson samples is again the signature for the presence of significant clumping of clusters at these scales. The functional m_1 shows also a positive deviation from the Poisson samples on scales ($35 \dots 50$) $h^{-1}\text{Mpc}$ where more coherent structures form in the union set than in the Poisson samples, keeping the surface density larger.

The Minkowski functionals m_2 and m_3 characterize in more detail the kind of spatial coverage provided by the union set of balls in the data sample. The density of the total mean curvature m_2 of the data reaches a maximum at about $10 h^{-1}\text{Mpc}$ produced by the dominance of convex (positive m_2) structures. The density m_2 at the maximum is reduced with respect to the Poisson sample to about 70% (or more than 3 standard deviations). The integral mean curvature m_2 has a zero at a scale of $25 h^{-1}\text{Mpc}$ (almost the scale of maximum of m_1) corresponding to the turning-point between structures with mainly convex and concave boundaries (negative m_2). Significant deviations from the Poisson distribution occur between this turning point and $40 h^{-1}\text{Mpc}$ due to the smaller mean curvature of the union set of the data, probably caused by the interconnection of the void regions in the cluster distribution.

The density of the Euler characteristic m_3 describes the global topology of the cluster distribution. On small scales all balls are separated. Therefore, each ball gives a contribution of unity to the Euler characteristic and m_3 is proportional to the cluster number density. As the radius increases, more and more balls overlap and m_3 decreases. At a scale of about $20 h^{-1}\text{Mpc}$ it drops below zero due to the emergence of tunnels in the union set (a double torus has $\chi = -1$). The positive maximum for the Poisson process at scales $\simeq 40 h^{-1}\text{Mpc}$ is the signature for the presence of cavities. The nearly linear decrease of the Euler characteristic for the Abell/ACO sample indicates strong clustering on scales $\lesssim 15 h^{-1}\text{Mpc}$. This confirms the results of Bahcall (1988), stating that superclusters consist mainly of pairs or triples of strongly correlated (rich) clusters. The lack of a significant positive maximum after the minimum shows that only a few cavities form. This suggests on such scales a support dimension for the distribution of clusters of less than three, (see also Borgani et al. 1993); note that the formation of cavities resulting in positive contributions to the Euler characteristic is not possible for a support dimension ≤ 2 . The presence of voids on scales of 30 to $45 h^{-1}\text{Mpc}$ is shown by the enhanced surface area m_1 and the reduced integral mean curvature m_2 , while on these scales the Euler characteristic m_3 is approximately zero. This does not confirm a pure shell model, proposed by Bahcall (1988) and used by Mecke, Buchert & Wagner (1994) as the ‘‘double Poisson process’’; rather, the shape of the cluster distribution is more likely described by a mixture of cavities and tunnels. However, since the scatter in the Minkowski functionals on scales above $45 h^{-1}\text{Mpc}$ is quite high, this last interpretation remains to be confirmed by larger future data sets.

4.5 Analysis of mock catalogues

Since the construction of mock samples by the algorithm described in Section 3 takes into account all selection effects of the Abell/ACO catalogue, we can analyze them by using the same procedure as for the real data. The considerable deviations of the mock samples’ number density from the mean cluster number density, as defined within the whole simulation box, are clearly seen

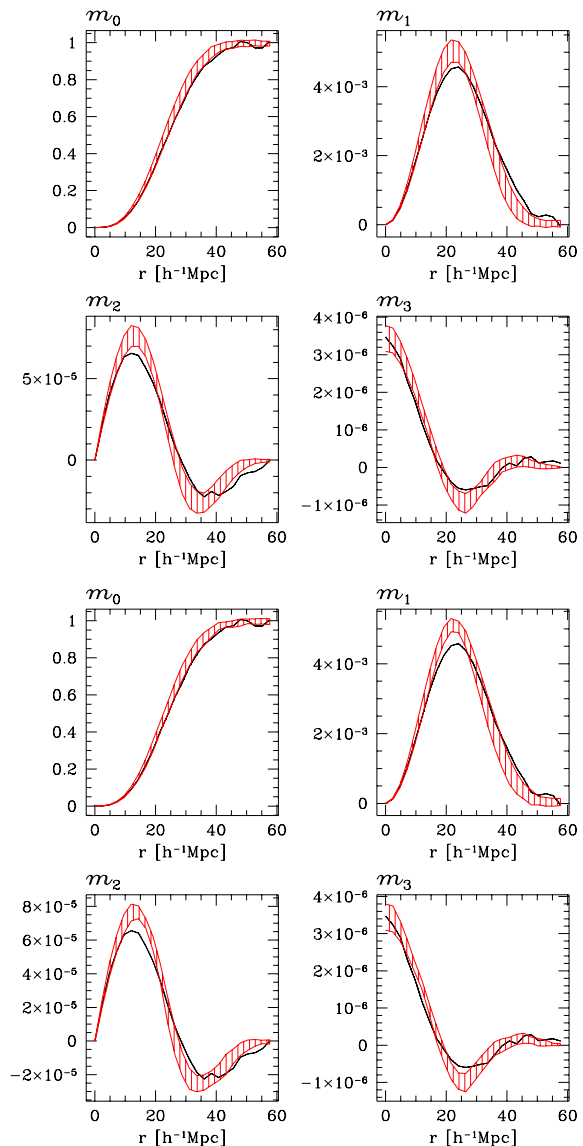


Figure 6. Densities of the Minkowski functionals for the Abell/ACO (solid line in both panels) compared to the SCDM (shaded area in top panel), and the TCDM (shaded area in bottom panel). The shaded area gives 1σ -errorbars of the variance among different realizations including cosmic variance, as explained in the text.

in the scatter of the density of the Euler characteristic m_3 at the smallest radii, which is proportional to the number density (see Figures 6 and 7). This suggests that even a sample as large as the Abell/ACO catalogue is not a ‘fair sample’ as discussed by Buchert and Martínez (1993), since it is still significantly influenced by cosmic variance.

A comparison of the four SCDM (or the three ΛCDM) realizations shows that this scatter in the number density is the main source for the variance seen in the Minkowski functionals. The statistical variance introduced by the scatter of different realizations of the initial density field is always negligible if compared to the observer-to-observer scatter in each box, associated

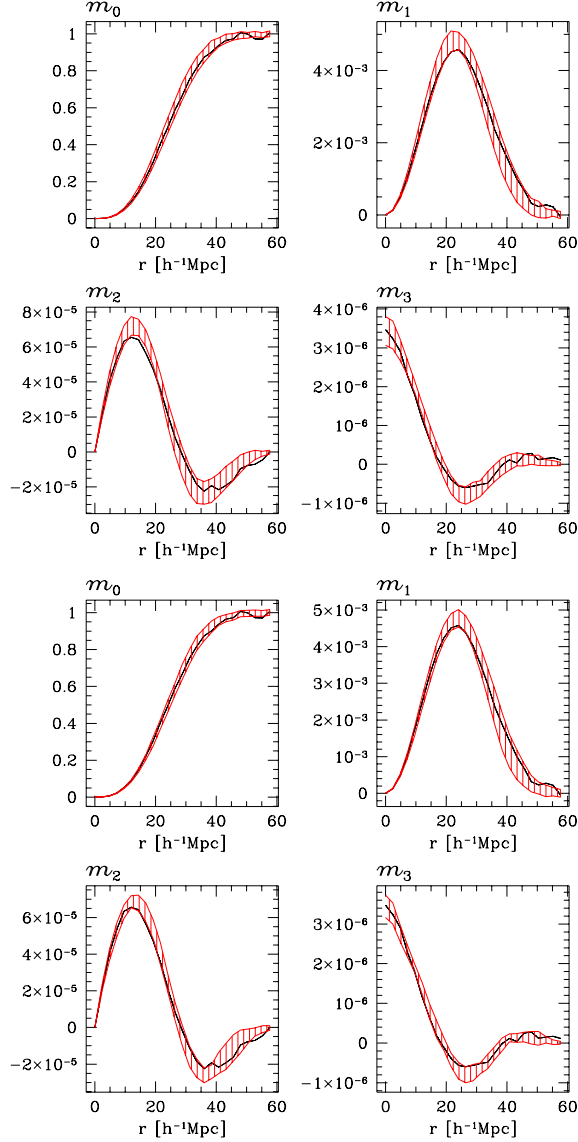


Figure 7. Densities of the Minkowski functionals for the Abell/ACO (solid line in both panels) compared to the Λ CDM (shaded area in top panel), and the BSI (shaded area in bottom panel). The shaded area gives 1σ -errorbars of the variance among different realizations including cosmic variance, as explained in the text.

with the number density fluctuations between different mock samples. In this sense the error bands shown in the plots include cosmic variance; only the ‘robustness’ (a result of the additivity property) and the high significance of the Minkowski functionals still allow for discrimination between the different Dark Matter cosmologies.

In Figure 6 we compare the densities of the functionals for SCDM and TCDM models to the Abell/ACO ones. Both models show too little clustering on small scales, as it is clearly seen by the enhanced maxima of the surface area m_1 and the integral mean curvature m_2 , as well as in the flatter decrease of the Euler character-

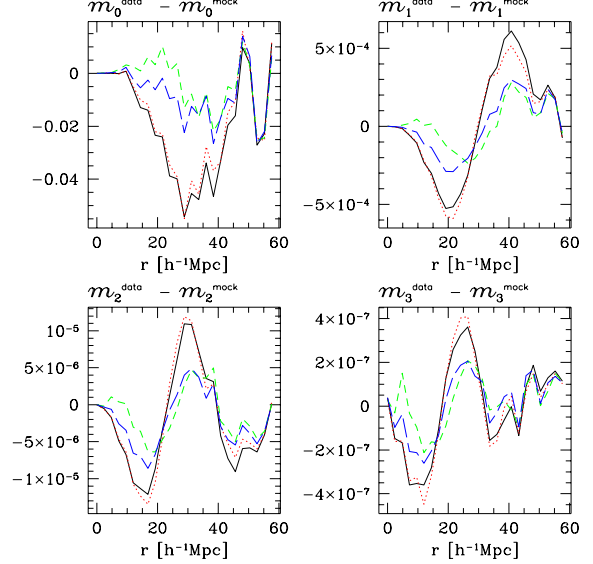


Figure 8. Differences of the densities of Minkowski functionals for the SCDM (solid line), TCDM (dotted), Λ CDM (long dashed), and the BSI (short dashed).

istic m_3 . Additionally, the higher volume m_0 indicates weak clumping also on large scales.

Figure 7 displays the same quantities as Figure 6 but for the Λ CDM and BSI models. Although small deviations from the Abell/ACO results are still present, again pointing towards weak clumping, both models perform much better than SCDM and TCDM.

This is also confirmed by the plot in Figure 8, where we show the differences between the functionals of the Abell/ACO data, m_μ^{data} , and the functionals of the mock samples, m_μ^{mock} . Again we see that Λ CDM and BSI describe the cluster distribution much better than SCDM and TCDM. At scales above $45 h^{-1}\text{Mpc}$ the differences between the Minkowski functionals of the Abell/ACO and the mock samples are dominated by random fluctuations in the Abell/ACO.

In order to quantify the statistical significance of these deviations we calculate the risks R_μ , with an error weighted quadratic cost function, for all functionals of all models versus those of the Abell/ACO sample. This risk is equal to the χ^2 distance used in maximum likelihood analysis (see e.g. Frieden 1991). For N_r radii it is given by

$$R_\mu = \sum_{i=1}^{N_r} \frac{(m_\mu^{\text{mock}}(r_i) - m_\mu^{\text{data}}(r_i))^2}{\sigma_\mu^{\text{mock}}(r_i)^2}, \quad (9)$$

where $\sigma_\mu^{\text{mock}}(r)$ is the standard error of the Minkowski functionals at radius r over several mock catalogues,

$$\sigma_\mu^{\text{mock}}(r) = \sqrt{\langle m_\mu^{\text{mock}}(r)^2 \rangle - \langle m_\mu^{\text{mock}}(r) \rangle^2}. \quad (10)$$

In Figure 9 we show the R_μ values for the four considered DM models. After excluding $r = 0$ and $r > 45 h^{-1}\text{Mpc}$, we limit the analysis to $N_r = 18$ radial bins. Therefore, a constant departure of 1σ should result in a risk $R_\mu = 18$, which is shown for reference in Fig-

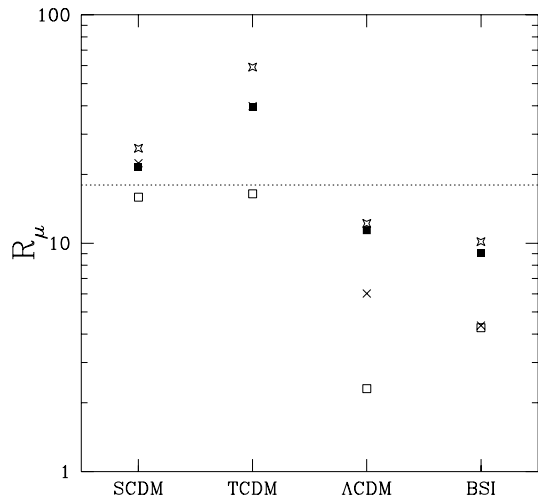


Figure 9. The risk values for simulations versus Abell/ACO for the volume measure R_0 (empty boxes), for the surface density R_1 (crosses), for the mean curvature R_2 (stars), and for the Euler characteristic R_3 (filled boxes).

ure 9 as a dotted line. SCDM shows a significant departure from Abell/ACO, as a result of the reduced clustering. The differences of TCDM are even larger than those of SCDM (cf. also Figure 8). The higher risk values for TCDM may be caused by underestimating σ_μ (we recall that we analyzed only one TCDM simulation, i.e. eight mock catalogues, but four SCDM simulation, i.e. 32 mock catalogues). As for Λ CDM and BSI, they are confirmed to fit the data much better; the difference with respect to Abell/ACO data is below the 1σ level for all the functionals, but showing also a tendency towards too weak clumping. The volume density (i.e. the void probability) alone is not sufficiently discriminating (see also Figures 6, 7), while the integral mean curvature m_2 is even more selective than the Euler characteristic m_3 .

5 SUMMARY AND CONCLUSION

We have calculated scale-dependent Minkowski functionals for spatial patterns induced by the point set of an Abell/ACO cluster redshift sample and compared these functionals with those obtained from a number of mock cluster catalogues obtained from different cosmological models. We find significant deviations in the morphological features of the observed cluster clumping from the Poisson distribution on scales $(15 \dots 50) h^{-1} \text{Mpc}$, which have not been explored previously in such detail. In particular, in the range $(15 \dots 45) h^{-1} \text{Mpc}$ the results indicate a clumping of clusters on a support with dimension less than three (see also Borgani et al. 1994). On scales $(25 \dots 45) h^{-1} \text{Mpc}$ the behavior of the Minkowski functionals m_1 (area), m_2 (integral mean curvature) and m_3 (Euler characteristic) may be interpreted as a cluster aggregation exhibiting cavities and interconnected tunnels

rather than isolated voids. Our results from the mock catalogues agree with the expectation that the SCDM and TCDM models do not describe the degree of cluster clumping as inferred from the data in the scale range $(15 \dots 45) h^{-1} \text{Mpc}$. Moreover the formation of cavity aggregates is not reproduced convincingly. On the other hand, the Λ CDM and the BSI models provide a reasonably good although not perfect description of the data.

The main source of uncertainty in the analysis arises from the fluctuations in the number density of objects among the mock catalogues. The deviations of the model results from the data are on the 1σ level. Nevertheless we think that the results are reliable, since they are inferred from the behaviour of our morphological measures over an extended range of the diagnostic length scale parameter r .

The family of Minkowski functionals focuses on global features of spatial patterns and includes, besides a topological descriptor for the connectivity, also geometrical measures for the size and shape. Thus the present approach provides a unifying frame for the analysis of cosmic structures which comprises the void probability function as well as the genus statistics; our method is introduced not to replace but to complement traditional tools such as low-order correlation functions.

The numerical code used for calculating the Minkowski functionals is available and can be obtained by sending e-mail to buchert@stat.physik.uni-muenchen.de.

ACKNOWLEDGEMENTS

MK and TB acknowledge support from the ‘‘Sonderforschungsbereich SFB 375 f ur Astroteilchenphysik der Deutschen Forschungsgemeinschaft’’. JR is supported by the Deutsche Forschungsgemeinschaft through grant Go563/5-2. SB, JS and MK thank the Astrophysical Institute of Potsdam for hospitality while preparing part of this work.

REFERENCES

- Abell G.O., 1958, ApJ, 3, 211
- Abell G.O., Corwin H.G., Olowin R.P., 1989, ApJS, 70, 1
- Amendola L., Gottl ober S., M ucket J.P., M uller V., 1995, ApJ, 457, 444
- Bahcall N.A., Soneira R.M., 1983, ApJ, 270, 20
- Bahcall N.A., 1988, Ann. Rev. Ast. Astroph., 26, 631
- Bahcall N.A., Cen R., 1992, ApJ Lett., 398, L81
- Bahcall N.A., West M.J., 1992, ApJ, 392, 419
- Bardeen J.M., Bond J.R., Kaiser N., Szalay A.S., 1986, ApJ, 304, 15
- Bennett C.L., Banday A., G orski K.M., Hinshaw G., Jackson P., Keegstra P., Kogut A., Smoot G.F., Wilkinson D.T., Wright E.L., 1996, ApJL, submitted, astro-ph/9601067
- Batuski D.J., Bahcall N.A., Olowin R.P., Burns J.O., 1989, ApJ, 341, 599
- Borgani S., Murante G., Valdarnini R., Provenzale A., 1993, Phys. Rev. E, 47, 3879

- Borgani S., Martínez V.J., Pérez M.A., Valdarnini R., ApJ, 1994, 435, 37
- Borgani S., Plionis M., Coles P., Moscardini L., 1995, MNRAS, 277, 1191
- Borgani S. et al., 1996, in preparation
- Buchert T., 1995, in Mückel J.P., Gottlöber S., Müller V., eds., p. 156, Large Scale Structure in the Universe, World Scientific, Singapore, astro-ph/9412061
- Buchert T., Martínez V.J., 1993, ApJ, 411, 485
- Cappi A., Maurogordato S., 1992, A&A, 259, 423
- Coles P., Davies A., Pearson R.C., 1996, MNRAS, in press, astro-ph 9603139
- Collins C.A., Guzzo L., Nichol R.C., Lumsden S.L., 1995, MNRAS, 274, 1071
- Croft R.A.C., Efstathiou G., 1994, MNRAS, 267, 390
- Dalton G.B., Croft R.A.C., Efstathiou G., Sutherland W.J., Maddox S.J., Davis M., 1994, ApJ, 271, L47
- Dubrulle B., Lachièze-Rey M., 1994, A&A, 289, 667
- Falconer K.J., 1990, Fractal Geometry. John Wiley & Sons, New York
- Fava N.A., Santaló L.A., 1979, Z. Wahrscheinlichkeitstheorie verw. Gebiete, 50, 85
- Frenk C.S., White S.D.M., Davis M., Efstathiou G., 1988, MNRAS, 235, 715
- Frieden B.R., 1991, Probability, Statistical Optics, and Data Testing, Springer, Berlin
- Ghigna S., Bonometto S.A., Retzlaff J., Gottlöber S., Murante G., 1996, ApJ, in press
- Górski K.M., Hinshaw G., Banday A.J., Bennett C.L., Wright E.L., Kogut A., Smoot G.F., Lubin P., 1994, ApJ, 430, L89
- Gott III J.R., Weinberg D.H., Melott A.L., 1987, ApJ, 319, 1
- Gottlöber S., Mückel J.P., Starobinsky A.A., 1994, ApJ, 434, 417
- Hadwiger H., 1957, Vorlesungen über Inhalt, Oberfläche und Isoperimetrie, Springer Verlag, Berlin
- Jing Y.P., Plionis M., Valdarnini R., 1992, ApJ, 389, 499
- Kates R., Müller V., Gottlöber S., Mückel J.P., Retzlaff J., 1995, MNRAS, 277, 1254
- Klypin A., Kopylov A.I., 1983, Soviet Astron. Lett., 9, 41
- Klypin A., Rhee G., 1994, ApJ, 428, 399
- Lacey C., Cole S., 1994, MNRAS, 271, 676
- Mecke K., Wagner H., 1991, J. Stat. Phys., 64, 843
- Mecke K., 1994, Integralgeometrie in der Statistischen Physik, Verlag Harri Deutsch, Thun, Frankfurt am Main
- Mecke K., Buchert T., Wagner H., 1994, A&A, 288, 697, astro-ph/9312028
- Melott A.L., 1990, Physics Rep., 193, 1
- Mo H.J., Jing Y.P., White S.D.M., 1996, submitted to MNRAS, astro-ph/9602052
- Nichol R.C., Briel U.G., Henry J.P., 1994, MNRAS, 265, 867
- Olivier S.S., Primack J.R., Blumenthal G.R., Dekel A., 1993, ApJ, 408, 17
- Peacock J.A., West M.J., 1992, MNRAS, 259, 494
- Pearson R., Coles P., Borgani S., Moscardini L., Plionis M., 1996, in preparation
- Peebles P.J.E., 1980, The Large-Scale Structure of the Universe, Princeton University Press, Princeton
- Platzöder M., Buchert T., 1995, in Weiss A., Raffelt W., Hillebrandt W., von Feilitzsch F., eds., Proc. 1st SFB Workshop on Astro-particle physics, Ringberg 1995, 251–263, astro-ph/9509014
- Plionis M., Valdarnini R., 1991, MNRAS, 249, 46
- Plionis M., Valdarnini R., Jing Y.P., 1992, ApJ, 398, 12
- Plionis M., Valdarnini R., 1995, MNRAS, 272, 869
- Postman M., Spergel D.N., Satin B., Juszkiewicz R., 1989, ApJ, 346, 588
- Postman M., Geller M.J., Huchra J.P., 1992, ApJ, 384, 404
- Rhoads J.E., Gott III J.R., Postman M., 1994, ApJ 421, 1
- Romer A.K., Collins C.A., Böhringer H., Cruddace R.G., Ebeling H., MacGillivray H.T., Voges W., 1994, Nature, 372, 75
- Schmalzing J., Kerscher M., Buchert T., 1995, in Bonometto S., Primack J., Provenzale A., eds., Proc. Int. School of Enrico Fermi, Course CXXXII, Varenna, in press, astro-ph/9508154
- Schneider R., 1993, Convex bodies: The Brunn–Minkowski theory, Cambridge University Press, Cambridge
- Stompor R., Górski K.M., Banday A.J., 1995, MNRAS, 277, 1225
- Stratonovich R. I., 1963, Topics in the theory of random noise, Vol.I, Gordon and Breach, New York
- Sutherland W., 1988, MNRAS, 234, 159
- Weil W., 1983, in Gruber et al., eds., Convexity and its applications, 360–412
- White S.D.M., 1979, MNRAS, 186, 145
- White S.D.M., Frenk C.S., Davis M., Efstathiou G., 1987, ApJ, 313, 505